A New Method and Mass Spectrometer Design for TOF-SIMS Parallel Imaging MS/MS

Gregory L. Fisher,[*,†] Anne L. Bruinen,[‡] Nina Ogrinc Potočnik,[‡] John S. Hammond,[†] Scott R. Bryan,[†] Paul E. Larson,[†] and Ron M.A. Heeren[‡]

[†]Physical Electronics, Inc., Chanhassen, Minnesota 55317, United States
[‡]Multi-Modal Molecular Imaging (M4I) Institute, Maastricht University, 6211 ER Maastricht, Netherlands

ABSTRACT: We report a method for the unambiguous identification of molecules in biological and materials specimens at high practical lateral resolution using a new TOF-SIMS parallel imaging MS/MS spectrometer. The tandem mass spectrometry imaging reported here is based on the precise monoisotopic selection of precursor ions from a TOF-SIMS secondary ion stream followed by the parallel and synchronous collection of the product ion data. Thus, our new method enables simultaneous surface screening of a complex matrix chemistry with TOF-SIMS (MS[1]) imaging and targeted identification of matrix components with MS/MS (MS[2]) imaging. This approach takes optimal advantage of all ions produced from a multicomponent sample, compared to classical tandem mass spectrometric methods that discard all ions with the exception of specific ions of interest. We have applied this approach for molecular surface analysis and molecular identification on the nanometer scale. High abundance sensitivity is achieved at low primary ion dose density; therefore, one-of-a-kind samples may be relentlessly probed before ion-beam-induced molecular damage is observed.
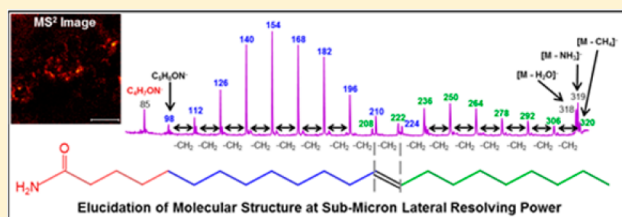
W hy don't biologists use secondary ion mass spectrometry (SIMS)?[1] It has been recognized for many years that tandem mass spectrometry (MS/MS or MS[n]) is required to identify peaks above ca. m/z 150 due to the limitations of mass resolution and mass accuracy in commercial time-of-flight SIMS (TOF-SIMS) instrumentation.[2] Numerous segments of industrial and academic researchers have gravitated toward methods of mass spectrometry imaging that can provide robust molecular identification by tandem mass spectrometry. However, the present tandem MS imaging designs, whether they employ primary ion beams[3,4] or laser beams[5,6] to generate ions for analysis, discard all ions except the precursor ions of interest when performing an MS/MS analysis. This constitutes an incredible loss of potentially useful information, particularly for biological applications.

A new TOF-TOF imaging mass spectrometer, exploiting the unique characteristics of the triple ion focusing time-of-flight (TRIFT) analyzer used in the PHI *nanoTOF* II, has been developed.[7] The spectrometer design allows for conventional TOF-SIMS (MS[1]) precursor ion analysis and tandem MS (MS[2]) product ion analysis of targeted precursor ions to be acquired simultaneously and in parallel. The secondary ions used for MS[1] and MS[2] imaging are produced from precisely the same analytical volume that is interrogated by the pulsed and digitally raster-scanned primary ion nanoprobe. This method of analysis, what we have called parallel imaging MS/MS, provides the maximum information from a given analytical volume. In this article, we demonstrate several unique attributes of TOF-SIMS parallel imaging MS/MS to identify the composition and structure of targeted molecular moieties at high lateral resolving power.

EXPERIMENTAL SECTION

Crystal Violet. Specimens of crystal violet were prepared by spotting a solution made of crystal violet powder (Ted Pella, California, U.S.A.) and HPLC grade methanol (VWR, Pennsylvania, U.S.A.) onto shards of natively oxidized silicon. The spotted solution was allowed to dry in ambient conditions prior to vacuum sample introduction and analysis. Alternatively, a black Sharpie permanent pen (U.S. trademark of Newell Rubbermaid), the ink of which contains a significant fraction of crystal violet, was used to mark clean shards of natively oxidized silicon.

Male Zebra Finch Brain Cross-Section. Fresh frozen male zebra finch (*T. guttata*) brain tissue (120 days post hatching), provided by the Bio-Imaging Laboratory, University of Antwerp, Belgium, was stored at −80 °C. The 12 μm-thick sagittal sections were produced using a cryo-microtome (Leica, Belgium) at −18 °C, thaw-mounted onto conductive indium—tin-oxide (ITO) slides (Delta Technologies, Texas, U.S.A.), and stored at −80 °C until analysis as described elsewhere.[8] Over a period of approximately 15 min prior to analysis, the tissue sections were dried and brought to ambient temperature in a desiccator.
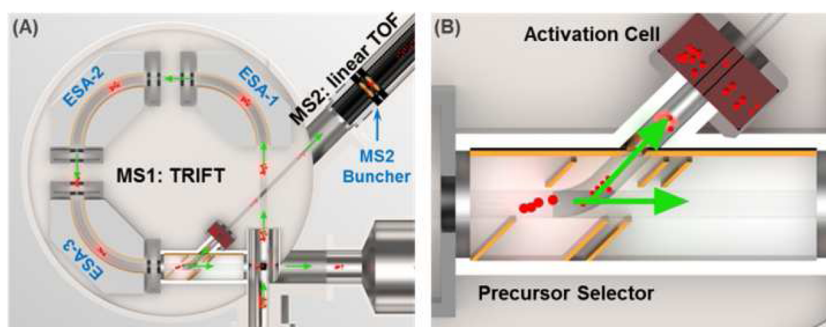
Figure 1. (A) Schematic illustration of the Parallel Imaging MS/MS spectrometer with the major MS1 (TRIFT) and the MS2 (linear TOF) components identified. The green arrows indicate the nominal trajectories of the secondary ions which are highlighted in red. The electrodynamic time compression elements (buncher) of the MS2 spectrometer are identified. The ion detectors of the spectrometers are not visible in the illustration. (B) A schematic illustration showing an enlargement of the precursor selector and the activation cell of the MS2 spectrometer.

Zebrafish Whole-Body Cross-Section. A female adult zebrafish (*D. rerio*) was infected by *M. marinum* (mutant strain *mptC*) and sacrificed as part of the study described by van der Sar and co-workers.[9] The whole fish was embedded in a mixture of 5% carboxy methylcellulose and 10% gelatin (Sigma-Aldrich, Zwijndrecht, Netherlands), frozen at −80 °C as previously described, and stored at −80 °C freezer overnight.[10] The block was cut into 20 μm-thick sagittal sections with a cryo-microtome (Microm HM 525, Microm International, Walldorf, Germany). A section showing severe infection was thaw mounted on an ITO-coated glass slide (Delta Technologies, Texas, U.S.A.). The slide was dried and brought to ambient temperature in a desiccator approximately 30 min prior to analysis.

Erucamide. Erucamide powder (Sigma-Aldrich, Missouri, U.S.A.) of >99% purity was dissolved in HPLC grade toluene (Sigma-Aldrich, Missouri, U.S.A.) and spotted onto a shard of natively oxidized silicon. The solution was allowed to dry in ambient conditions prior to vacuum sample introduction and analysis.

TOF-SIMS Analysis. All TOF-SIMS parallel imaging MS/MS analyses were performed using a prototype TRIFT spectrometer on a PHI *nanoTOF* II TOF-SIMS instrument (Physical Electronics, Minnesota, U.S.A.) that is equipped with a 30 kV Bi_n^{q+} cluster liquid metal ion gun (LMIG). The LMIG column was operated such that the sample was interrogated by a mass pure Bi_3^+ cluster ion beam. The dc current of the primary ion beam was 12 nA for the biological analyses and 6 nA for the materials' analyses. The analytical field-of-view (FOV), in all cases using 256 × 256 image pixels, was varied depending on the analysis; however, the primary ion dose density (PIDD) never exceeded a static limit of 5.0 x10^{12} ions/cm^2. The gas pressure in the CID activation cell cannot be measured directly but was monitored by a nearby gauge in the TRIFT spectrometer. In the course of each acquisition, mass spectral information at each image pixel was collected at 8300 Hz, in the range of m/z 0−1850, and saved into a raw data stream file. Saving complete mass spectra at each image pixel allows off-line data reduction and data mining (i.e., retrospective analysis). Charge compensation was achieved using 15 eV electrons and 10 eV Ar$^+$ ions. All samples were nominally held at room temperature throughout the analyses. The images and spectral data presented herein were produced from the raw data files using PHI SmartSoft-TOF and PHI TOF-DR (Physical Electronics, Minnesota, U.S.A.) software. The data have not been conditioned in any way with the exception of intensity scaling by adjusting the lower or upper intensity threshold.

RESULTS AND DISCUSSION

Instrumental Design. The parallel imaging MS/MS spectrometer is based on the TRIFT ion microscope discussed by Schueler and colleagues.[11,12] There is a unique spatial crossover after the third electrostatic analyzer (ESA), as illustrated in Figure 2 (ref 12), wherein the secondary ions have reached almost complete time-of-flight separation. This position in the spectrometer provides an unique opportunity to deflect a temporally narrow, spatially focused, mass-resolved packet of ions into a second spectrometer for further analysis. In the parallel imaging MS/MS spectrometer design, a precursor selection device has been positioned at the spatial-temporal crossover after the third ESA of the MS1 (TRIFT) spectrometer.[7] The precursor selector window has a resolution of 1 Da (Da) at m/z 500. It is possible that more than one molecular precursors exist within the precursor selection window. The 1 Da precursor selection of the present design is much narrower than commonly used designs which are typically in the range of 4 to 10 Da. Therefore, interpretation of the resulting product ion spectra, even if precursor interferences exist, is simplified and does not require extraordinary performance in mass resolution or mass accuracy.

The selected precursor ions are deflected immediately at ≈1.5 keV into a collisional activation cell having a length of approximately 60 mm.[7] The argon gas pressure in the activation cell is estimated to be 1000× greater than that of the TRIFT spectrometer, which is measured to be 1.0×10^{-5} Pa when the collision gas valve is open. The percent duty cycle of the precursor selector is variable by the operator such that, if desired, a fractional portion of the precursor ions may remain in the MS^1 spectrum for the purposes of calibration, normalization, or quantification. Peaks in the MS^1 spectrum that are within m/z ± 3 of the precursor centroid mass suffer a loss of mass resolution and mass accuracy; this effect is negated if the precursor duty cycle is other than 100% (i.e., if some precursor signal is selected to remain in the MS^1 spectrum). The entire TOF-SIMS (MS^1) spectrum, less all or part of the precursor ions, is acquired in the standard way at the MS1 detector. The selected precursor and fragment ions that emerge from the activation cell are electrodynamically bunched and postaccelerated into a linear TOF mass spectrometer (MS2) where the product ion (MS^2) spectrum is collected at the MS2 detector. The essential features of the parallel imaging MS/MS
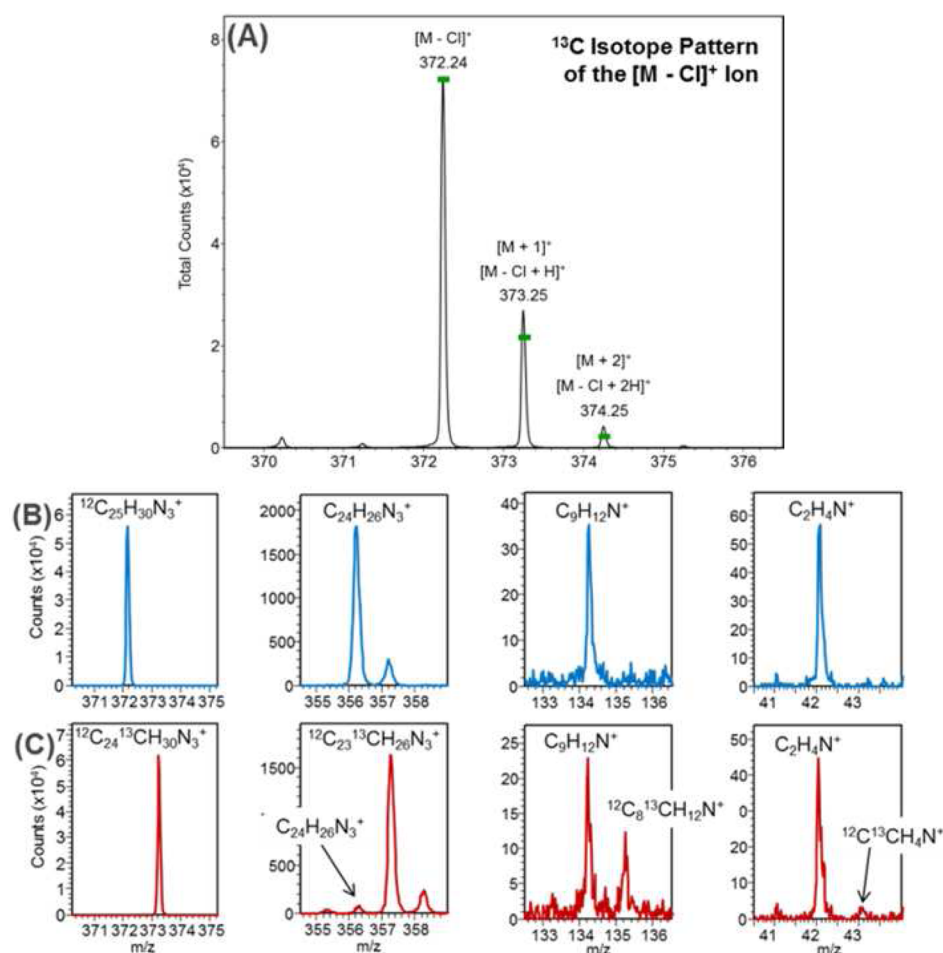
Figure 2. (A) MS^1 mass spectrum, in the range of m/z 370–376, showing the ^{13}C isotope pattern of the $[M − Cl]^+$ quasi-molecular ion of crystal violet. The green bar markers indicate the expected isotope signals based on the calculated ^{13}C content. (B) MS^2 spectra demonstrating a 1 Da precursor ion selection window at the $[M − Cl]^+$ quasi-molecular ion of crystal violet. The successive panels show MS^2 product ions of the $[M − Cl]^+$ precursor at several nominal masses. (C) MS^2 spectra demonstrating a 1 Da precursor ion selection window at the $[M + 1]^+$ quasi-molecular ion of crystal violet. The successive panels show MS^2 product ions of the $[M + 1]^+$ precursor at several nominal masses.

spectrometer, and of the assembly comprising the precursor ion selector with the activation cell, are shown schematically in Figure 1. To be clear, MS1 is defined as the TRIFT ion optics and detector, and MS^1 is defined as the imaging mass spectrometry data produced in MS1. Likewise, MS2 is defined as the tandem linear TOF ion optics and detector, and MS^2 is defined as the tandem imaging mass spectrometry data produced in MS2.

From this brief description, two unique characteristics of the parallel imaging MS/MS over existing tandem MS imaging designs become apparent. First, no ions are discarded or precluded from detection in any given tandem MS imaging analysis. Second, the synchronous nature of the parallel imaging MS/MS analysis provides an internal calibration of the MS^2 spectrum against the MS^1 spectrum; therefore, there is never a need for an applied (i.e., exogenous) reference. Other advantages include a sampling depth of only $\approx$2 nm, high abundance sensitivity at very low primary ion dose density (i.e., nondestructive analysis), and submicron to 100 nm lateral resolving power. An ionization matrix as used in MALDI is not routinely employed in TOF-SIMS analysis, and therefore, the endogenous molecular chemistry may be targeted for characterization without the interferences associated with an applied ionization matrix.

Crystal Violet. The $+m/z$ 372 precursor ion from a sample of crystal violet was selected for tandem MS characterization. The composition of the m/z 372 precursor is known to be $C_{25}H_{30}N_3^+$, corresponding to the $[M − Cl]^+$ ion of the crystal violet salt, and is often used as a standard for high mass optimization in TOF-SIMS analysis. The product ion spectrum of the m/z 372 precursor confirms a $C_{25}H_{30}N_3^+$ composition. The root-mean-square (RMS) mass deviation of the product ions comprising the MS^2 calibration is 3.19 mDa, and the mass accuracy (W) calculated at the precursor is 5.85 ppm.

An expansion of the MS^1 spectrum about the $[M − Cl]^+$ molecular ion peak of crystal violet, m/z 370–376, is given in Figure 2A. The bars (green) indicate the expected intensity of peaks containing one or more atoms of the ^{13}C isotope. The $[M + 1]^+$ peak contains one ^{13}C atom, while the $[M + 2]^+$ peak contains two ^{13}C atoms. The intensity of the $[M + 1]^+$ and $[M + 2]^+$ peaks is somewhat greater than expected based on the ^{13}C content alone, and the additional signal intensity arises from the addition of hydrogen to the $[M − Cl]^+$ ion (i.e., $[M − Cl + H]^+$ and $[M − Cl + 2H]^+$, respectively); this is a common observation in TOF-SIMS analysis owing to the use of keV ion probes.

The spectra shown in Figure 2B reveal the capability to set a 1 Da precursor ion selection window for parallel imaging MS/
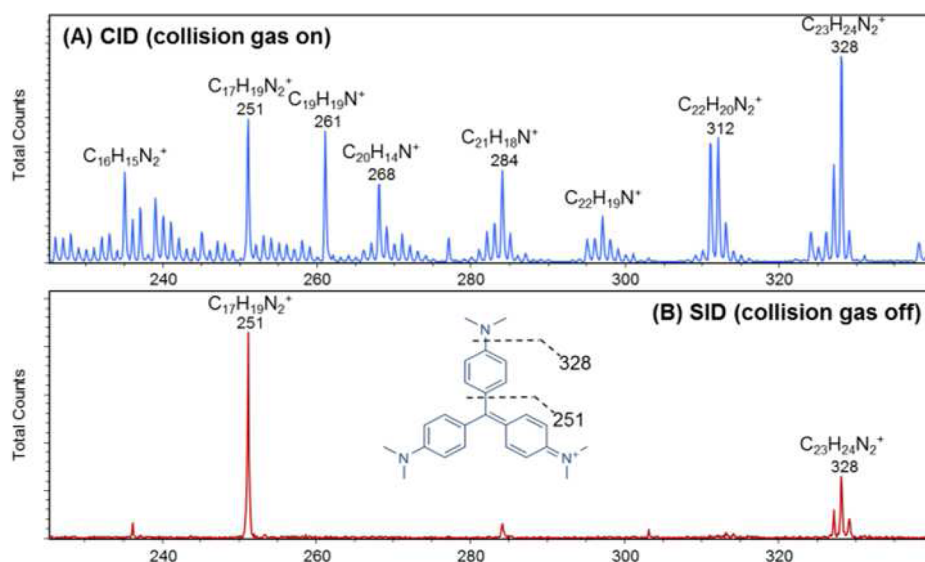
Figure 3. (A) MS^2 product ion spectrum produced by CID of the [M − Cl]$^+$ precursor of crystal violet (m/z 372) with annotation of the major product ions. (B) MS^2 product ion spectrum produced by SID of the [M − Cl]$^+$ precursor of crystal violet (m/z 372) with annotation of the major product ions. The inset shows the intact functional group neutral loss cleavages that give rise to the $C_{23}H_{24}N_2^+$ (m/z 328) and the $C_{17}H_{19}N_2^+$ (m/z 251) products.

MS. The [M − Cl]$^+$ precursor, or $C_{25}H_{30}N_3^+$, is observed in the top-left panel. In each panel to the right, neutral losses from the [M − Cl]$^+$ precursor ions produce the observed product ions. The $C_{24}H_{26}N_3^+$ product at m/z 356 arises by neutral loss of CH_4, while the product at m/z 357 arises by a less favored neutral loss of CH_3. The $C_9H_{12}N^+$ product at m/z 134 is produced by neutral loss of two N,N-dimethylaniline groups from the [M − Cl]$^+$ precursor. The $C_2H_4N^+$ product at m/z 42 is generated by cleavage between a dimethyl amine and a phenyl ring of the [M − Cl]$^+$ precursor. Note that all product ions contain only ^{12}C atoms. This observation can only be appreciated when compared to the product ion spectrum of the [M + 1]$^+$ precursor.

The spectra shown in Figure 2C provide an overview of the [M + 1]$^+$ product ion spectrum (i.e., the [M − Cl]$^+$ precursor ions containing one ^{13}C atom). The [M + 1]$^+$ precursor, or $^{12}C_{24}^{13}CH_{30}N_3^+$, is observed in the bottom-left panel; note that there is no signal arising from the $C_{25}H_{30}N_3^+$ precursor. In each panel to the right, the same neutral losses described above produce the observed product ions. However, the probability either of the neutral loss or of the product to contain the single ^{13}C atom depends on how many atoms are present in the neutral loss or the remaining product. The greater the number of carbon atoms, the greater the probability of that moiety to contain the ^{13}C atom. The $^{12}C_{23}^{13}CH_{26}N_3^+$ product at m/z 357 arises by neutral loss of $^{12}CH_4$, while the product at m/z 358 arises by a less-favored neutral loss of $^{12}CH_3$. The $^{12}C_8^{13}CH_{12}N^+$ product at m/z 135 is produced by neutral loss of two N,N-dimethylaniline groups from the [M + 1]$^+$ precursor. The strong signal of $C_9H_{12}N^+$ at m/z 134 occurs because there is a high probability that the ^{13}C atom is part of the neutral loss. Finally, there is only a diminutive signal of the $^{12}C^{13}CH_4N^+$ product at m/z 43, and a much greater signal of the $C_2H_4N^+$ product at m/z 42, because the ^{13}C atom is most often contained in the neutral loss.

Product ion spectra are most often generated by fragmentation of the precursor ions in an activation cell filled with a partial pressure of Ar gas. We have found that the relative intensities of the product ions change very little with a change in gas pressure of approximately an order of magnitude; however, there is a maximum pressure at which all product ion intensities begin to attenuate. It is possible to quantify a combination of the MS2 ion transmission and the conversion of precursor ions to product ions in a metric designated as the precursor conversion efficiency (P_{CE}). The P_{CE} value, in percent (%), is calculated from a ratio of the integrated counts of all product ions in MS^2, excluding unfragmented precursor ions in MS^2, over the integrated counts of the precursor ions in MS^1, normalized by the primary ion dose and multiplied by 100. We find on average that P_{CE} is >25% in both the positive and the negative ion polarities, but P_{CE} is molecule dependent and has been measured for numerous precursors to range from 0.5% to a high of over 75%.

It has also been noticed, as exemplified in Figure 3B, that surface-induced dissociation (SID) of the precursor ions may occur when there is no collision gas in the activation cell. A review of precursor ion activation and dissociation methods (Sleno and Volmer, 2004) includes an overview of SID.[13] Considering the precursor selector and activation cell geometry in the parallel imaging MS/MS spectrometer, it is surmised that SID occurs by grazing incidence of the precursor ions at the walls of the activation cell. For comparison to the SID product ion spectrum, the CID product ion spectrum is provided in Figure 3A. The CID spectrum of the crystal violet [M − Cl]$^+$ precursor (m/z 372), with the m/z 225−340 range displayed, reveals rather complete fragmentation of the [M − Cl]$^+$ precursor at each molecular bond. The strongest peaks are those corresponding to energetically favored neutral losses, but the abundance of product ion peaks indicates that energetically unfavorable neutral losses also occur. It is not likely that any rearrangement products are observed in the CID product ion spectrum due to both the high velocity of the 1.5 keV collisions and the short duty cycle of the TOF-TOF analysis (e.g., 120 μs in MS^1 and 52 μs in MS^2). The SID spectrum, on the other hand, contains only neutral losses of intact functional groups indicating a more gentle fragmentation mechanism. The mass
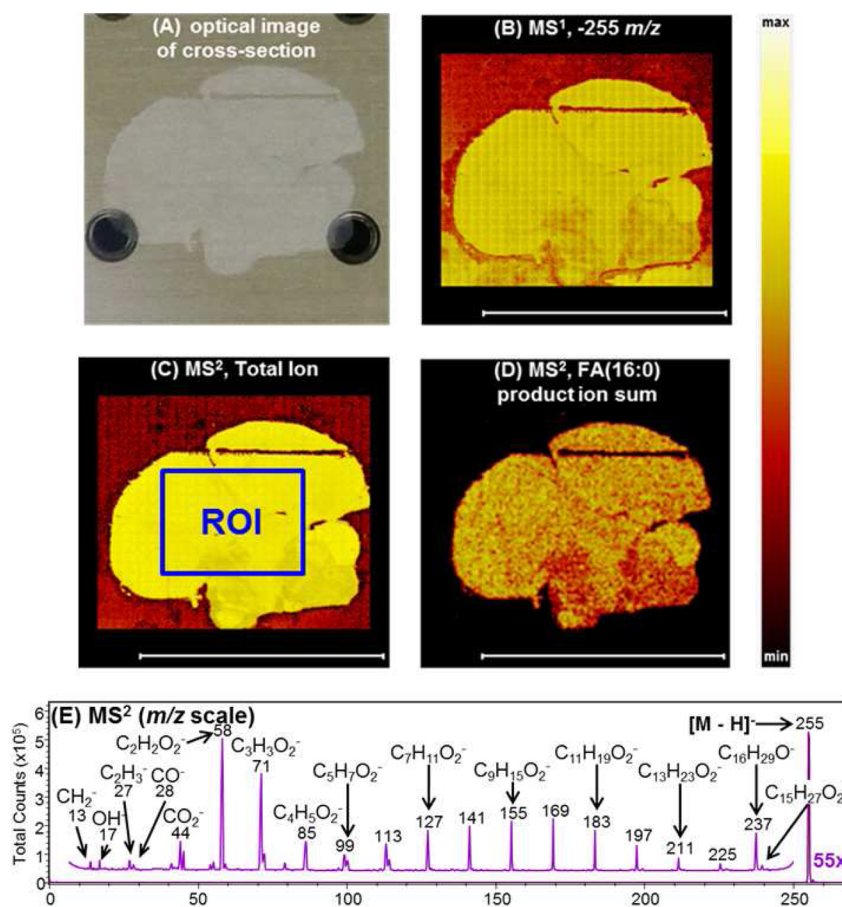
Figure 4. (A) Optical navigation image of a sagittal section from a wild-type adult male zebra finch brain. (B) Log-scale MS^1 image at $-m/z$ 255. (C) Log-scale MS^2 total ion image of the $-m/z$ 255 precursor. This image is a sum of all CID product ions and the unfragmented precursor ions. The region-of-interest (ROI) from which spectral information was generated is shown. (D) Log-scale MS^2 image of FA(16:0) $[M - H]^-$ CID product ions. This image is a sum of product ions at m/z 58, 71, 141, 155, and 169. The image areas are 11.2 mm × 9.6 mm; the scale markers are 10 mm. (E) The CID product ion spectrum of the $-m/z$ 255 precursor from an ROI of the zebra finch brain section.

deviation of the SID product ion spectrum is calculated to be 4.31 mDa RMS and the mass accuracy calculated at the precursor is 3.44 ppm, so we have high confidence in the product ion compositions.

In general, the mass resolution $(m/\Delta m_{fwhm})$ in MS^2 is specified to be ≥2000 at the precursor. From the MS^2 spectrum of crystal violet, we measure $m/\Delta m$ = 1668 at m/z 28 of the CH_2N^+ product and we measure $m/\Delta m$ = 3990 at m/z 372 of the $[M - Cl]^+$ precursor. An interesting revelation is that the MS^2 mass resolution increases as a function of mass-to-charge ratio which is a circumstance not typically observed in tandem mass spectrometry. We postulate that this phenomenon is a consequence of ion scattering from Ar gas and from neutral fragments in the CID activation cell. The result is that smaller, less massive product ions have a greater angular distribution but larger, more massive product ions and intact precursor ions have a relatively narrow angular distribution. Ions with a greater angular dispersion (i.e., those of decreasing mass-to-charge ratio) will necessarily have a larger time (velocity) spread upon arriving at the detector which will result in poorer mass resolution.

By operating the TOF-TOF spectrometer in the product ion scan mode, we achieve simultaneous surface screening of the matrix components by MS^1 imaging and targeted identification of matrix components by MS^2 imaging. Such a statement is fully appreciated in light of the crystal violet data which

demonstrates great selectivity of the precursor ions. The targeted analysis afforded by the 1 Da (monoisotopic) precursor selection window reduces significantly the demand for high mass resolution in the MS^2 spectrum. This circumstance arises because a narrow precursor window eliminates the chemical interferences that drive the need for ultrahigh mass resolution. Any chemical interferences present in the 1 Da precursor window simply fall out, or become obvious, in the product ion spectrum. Likewise, the narrow precursor window produces greater abundance sensitivity in MS^2 because the spectral background, arising predominantly from postsource decay (PSD) of metastable ions, is eliminated.

Zebra Finch Brain Cross-Section. Lipids and metabolites play an important role in the early stages and progression of neurodegenerative diseases, neuro-plasticity, and ontogenesis.[14−18] In the male zebra finch brain, we have the opportunity to study anatomical and neurochemical changes that occur as part of the song learning behavior. Several studies, one including the use of TOF-SIMS, indicate that fatty acid distributions play a critical role in the song-learning process.[19−22] Our experiments provide for the first time the proper molecular identification of lipid and fatty acid species in the discrete nuclei and neuronal connections of the song-learning pathway. All analyses were performed on a single cross-section of brain tissue.
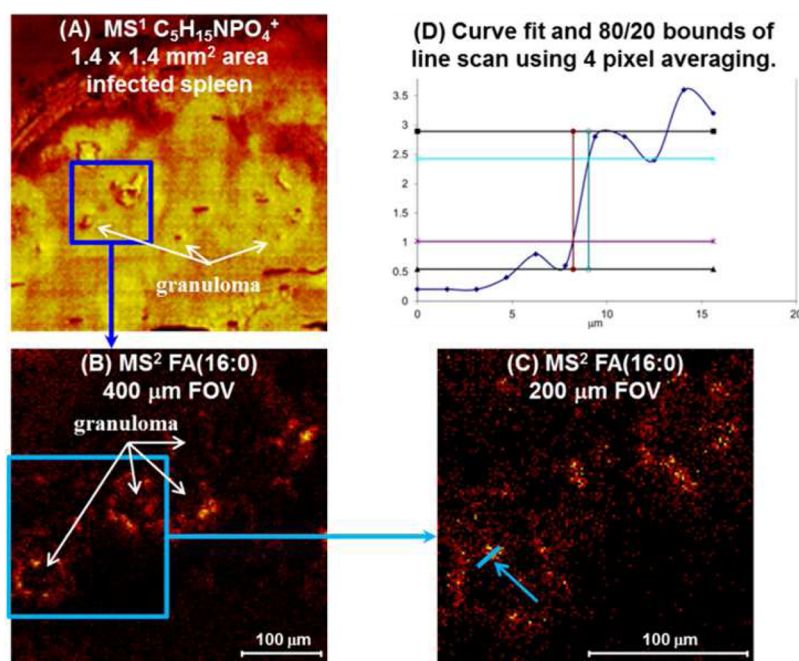
Figure 5. (A) Linear-scale MS^1 mosaic map of the phosphocholine headgroup ($C_5H_{15}NPO_4^+$), having dimensions of 1.4 mm × 1.4 mm, within the diseased zebrafish spleen. Several granulomata are indicated by arrows. The box indicates a region containing several granulomata and from which a zoom image is produced. (B) An MS^2 mosaic zoom image of the FA(16:0) $[M − H]^-$ distribution surrounding the necrotic core of the granulomata. The 400 μm FOV corresponds to an 8× zoom of the mosaic map. (C) An MS^2 product ion image of the FA(16:0) $[M − H]^-$ precursor, at 16× zoom of the mosaic map, wherein individual cells are distinguished. The line scanned feature, with 4 pixel averaging, is shown. (D) The line scan reveals a lateral resolving power ($\Delta l_{80/20}$) of 0.8 μm.

Several sulfatides, phospholipids, sterols, and fatty acids have been identified as the main molecular participants within discrete song-learning nuclei and the neuronal connections between the nuclei. This example illustrates the utility of simultaneous screening of complex biological chemistry by MS^1 imaging and the targeted identification of biological molecules by MS^2 imaging. It is overwhelmingly the case that biological components cannot be identified with MS^1 alone, so MS^2 is employed for targeted identification. That is to say, MS^1 provides the capability to separate the components of the complex mixture for parallel identification with MS^2. The very high signal-to-noise (S/N) of MS^2, combined with a 1 Da precursor selection window, provide the basis for targeted identification.

An optical image of a sagittal section from a male zebra finch brain is shown in Figure 4A as it was mounted on the sample stage and introduced for analysis. A large area (stage raster) mosaic map of 11.2 mm × 9.6 mm was collected from the tissue section at four primary ion beam pulses per pixel resulting in a primary ion dose density (PIDD) of $3.68 × 10^{10}$ Bi_3^+/cm^2. Both MS^1 and MS^2 image data were collected simultaneously in the negative ion polarity. A log-scaled MS^1 image of the $−m/z$ 255 precursor, ostensibly the $[M − H]^-$ molecular ion of palmitic acid ($C_{15}H_{31}CO_2H$), is given in Figure 4B. There is high signal at m/z 255 observed from the ITO substrate surrounding the tissue section. It is possible that thaw mounting has caused biomolecules to bleed onto the surrounding substrate. The log-scaled MS^2 total ion image presented in Figure 4C also reveals a noticeable ion signal from the surrounding ITO substrate. The fragment ion spectrum from a region-of-interest (ROI) on the tissue was characterized, displayed in Figure 4E, and confirms a predominance of FA(16:0), palmitic acid. Confidence in the spectral assignments

is established by the resulting spectral mass deviation of 2.18 mDa RMS and the calculated mass accuracy of 2.17 ppm at the precursor. With confidence in the MS^2 peak assignments, an image sum of identified $C_{15}H_{31}CO_2^-$ product ions can be used to generate an MS^2 image. A log-scaled MS^2 image sum of product ions (i.e., including only the peaks at m/z 58, 71, 141, 155, and 169) of the $C_{15}H_{31}CO_2^-$ precursor, displayed in Figure 4D, reveals that the palmitic acid detected in MS^2 is localized to the biological tissue.

Zebrafish Whole-Body Cross-Section. As part of an ongoing tuberculosis study, we have probed the role of lipids and metabolites in the disease states of zebrafish (*D. rerio*) that have been infected with *M. marinum*.[9] These bacteria initiate a granulomatous inflammation similar to the disease progression of tuberculosis in humans. We have focused our analyses on the spleen of a severely inflamed adult zebrafish containing many granulomata. All analyses have been conducted on a single whole-body zebrafish cross-section. Dozens of repeat analyses can be performed by TOF-SIMS parallel imaging MS/MS with minimal damage or consumption of the sample. We have observed that the abundance of certain lipids, sterols, and fatty acids appear to differ, specific molecules being either elevated or depressed in the diseased tissue. For instance, in the presumably necrotic cells of the granulomata, we notice elevated signals of the palmitic acid FA(16:0) molecular ion ($C_{16}H_{31}O_2^-$, m/z 255). For the purposes of brevity, we dispense with displaying a majority of the MS^1 and MS^2 data used to image the molecular distributions and to confirm the precursor composition(s) because this will be reported fully in a separate paper. The discussion here will focus on the demonstration of submicron MS^2 imaging and molecular identification by the analysis of *M. marinum* infection in zebrafish.
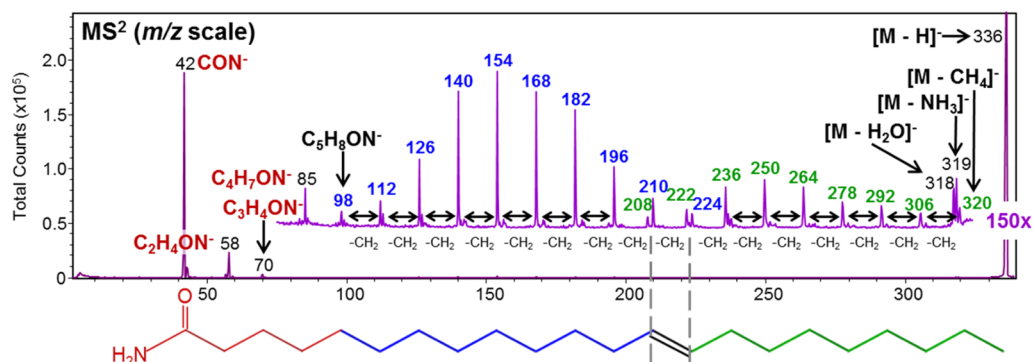
Figure 6. CID product ion spectrum of the −*m/z* 336 precursor produced from a spotted reference of erucamide. The C═C double bond is clearly identified at the Δ^{13} position. A stick model of the erucamide molecule is shown below the MS² spectrum, and the model has been scaled such that each molecular carbon atom is matched with the corresponding spectral feature.

A mosaic map having dimensions of 4.8 mm × 3.2 mm, encompassing the spleen, was collected from the zebrafish section using five primary ion beam pulses per pixel. The PIDD was 4.60×10^{10} Bi_3^+/cm^2 and was delivered by a primary ion beam with a dc current of 12 nA. Both MS¹ and MS² image data were collected simultaneously in the negative ion polarity. For clear observation of the diseased zebrafish spleen and the granulomata within, an MS¹ image of the phosphocholine headgroup ($C_5H_{15}NPO_4^+$, *m/z* 184) is rendered in Figure 5A. The MS¹ phosphocholine image has been cropped from a larger mosaic map, acquired in a separate analysis, to highlight the desired region of the spleen. The granulomata are clearly visible in this image, and a few are labeled for ease of identification. A region surrounding a few of the granulomata has been identified in Figure 5A, and this area is one region of focus for MS² imaging of fatty acids. Fatty acid identification and distribution is of interest because fatty acids are thought to be metabolized from intact lipids by the *M. marinum* bacteria. MS² imaging is necessary because the distribution of a targeted molecular chemistry is desired, and targeted analysis by MS¹ imaging alone has a number of uncertainties.

An 8× zoom of the MS² mosaic map of the negative ion FA(16:0) precursor ([M − H]⁻, *m/z* 255) is given in Figure 5B; the approximate location of this image area is highlighted on the $C_5H_{15}NPO_4^+$ image of Figure 5A. At this zoom level, a 400 μm FOV image area is produced, and several granulomata may be observed. A 16× zoom produces a 200 μm FOV MS² product ion image of the FA(16:0) [M − H]⁻ precursor, given in Figure 5C, wherein cells begin to be individually distinguished. To measure the lateral resolution, a line scan with 4 pixel averaging was made across several features. An example line scan is identified in Figure 5C, and the fit is plotted in Figure 5D. The measurement reveals a practical lateral resolution ($\Delta l_{80/20}$) of 0.8 μm. We have shown in other articles that, with different operating conditions of the analytical ion beam, a lateral resolving power of <200 nm may be achieved for both MS¹ and MS² imaging.[23,24]

Erucamide. The presence of unsaturation in molecules is readily discerned in the MS² spectrum because the keV CID produces, in many cases, complete fragmentation of the molecular precursor ions.[6] Additionally, unimolecular rearrangement of the CID products are not likely given the high velocity of the 1.5 keV ions and the high frequency operation (8300 Hz) of the MS2 spectrometer. We first noted the effects of unsaturation in the product ion spectra generated from stearic acid, FA(18:0), and from oleic acid, FA(18:1), which are

present in practically all biological specimens. The sensitivity toward and characterization of molecular double bonds is illustrated in Figure 6 wherein is given an MS² spectrum of erucamide. Erucamide is a polymer additive that contains a Δ^{13} unsaturation. The negative polarity product ion spectrum of the [M − H]⁻ precursor at *m/z* 336 was obtained from a spotted sample of the pure reference material. A spectral mass deviation of 6.79 mDa RMS and a calculated mass accuracy of 3.70 ppm at the precursor provide high confidence in the compositional peak assignments.

As recorded in Figure 6, each product ion in the MS² spectrum is clearly identified. Starting at the [M − H]⁻ precursor, we observe a CH_4 neutral loss resulting in the $C_{21}H_{38}ON^-$ product at *m/z* 320 followed by a series of methylene neutral losses resulting in the $C_{15}H_{26}ON^-$ product at *m/z* 236. From *m/z* 236, we see two additional methylene neutral losses, with decreasing signals, at *m/z* 222 ($C_{14}H_{24}ON^-$) and at *m/z* 208 ($C_{13}H_{22}ON^-$). There is another series of methylene neutral losses beginning at *m/z* 224 ($C_{14}H_{26}ON^-$), with increasing signals, to *m/z* 210 ($C_{13}H_{24}ON^-$), *m/z* 196 ($C_{12}H_{22}ON^-$), and so on. The intersection of these overlapping series of methylene neutral losses result in a doublet appearing in the MS² spectrum about the Δ^{13} unsaturation between C_{13} and C_{14}. The intersection of the neutral loss series at the molecular C═C double bond is reinforced by the illustration of the erucamide molecule in Figure 6. Hence, the keV CID has provided structural detail which is observed at high signal-to-noise (S/N). The mechanism of product ion formation likely occurs by charge-associated fragmentation (ref 25), which agrees well with our observations of unsaturation in both the positive ion and the negative ion polarities.[25]

■ CONCLUSION

The advantages of mass spectrometry imaging in addressing questions of biological and materials chemistry are well-documented.[26−29] The use of MS imaging in biological research has been dominated by MALDI-TOF while TOF-SIMS, presently at the fringes of biological research, has been of modestly growing interest. The specific attributes of TOF-SIMS that contribute to its allure include submicron to below 100 nm lateral resolution, high abundance sensitivity, high data collection rate, and excellent reproducibility because an applied matrix is not typically employed.[1] However, TOF-SIMS is often bemoaned for the inability to elucidate the identification of intact molecules.[1,26,29] This historical limitation of TOF-SIMS

is due to insufficient mass resolution and mass accuracy at $>m/z$ 150.

Cerruti and co-workers recently explained that a new MS imaging capability is sorely needed.[28] They state that while high mass resolution is an attractive feature of some ion trap and quadrupole-based tandem MS instruments, the shortcoming is either a large precursor selection window or a narrow precursor selection window but with poor sensitivity. Moreover, the duty cycle of ion trap devices is often not amenable to imaging. Continuing, they state that new instrument designs of practical utility for biological imaging and molecular characterization should have high mass resolution on the precursor selection, high lateral resolution, and high energy collisional activation. The new TOF-SIMS parallel imaging MS/MS spectrometer we have described and demonstrated in this paper unites all of the desired qualities of a mass spectrometry imaging capability for the characterization of biological molecules (sans proteins) directly from a tissue or even from single cells. We have demonstrated this new tandem mass spectrometry imaging capability to be of broad application in materials characterization as well as biological applications. Surpassing the basic functional requirements as espoused by Cerruti and colleagues, the new method and spectrometer design reported here allows the parallel and lossless collection of the MS^1 and the MS^2 data sets so that no ions are discarded, and the maximum information is extracted from the analytical volume. This inherent functionality is an advantage because the MS^1 spectrum often presents a convenient means to confirm MS^2 peak assignments and vice versa and, additionally, enables the potential use of the MS^1 data for normalization or quantification. We believe this new technology and method will find broad application and use in polymers and additives, forensics, high performance materials, biology, pharmaceuticals, pathology, prosthetics and medical implants, food sciences, cosmetics, discovery and failure analysis.

■ AUTHOR INFORMATION

Corresponding Author
*E-mail: gfisher@phi.com. Phone: +1 952 828 6460. Fax: +1 952 828 6451.

Notes
The authors declare no competing financial interest.

■ ACKNOWLEDGMENTS

■ REFERENCES

(1) Heeren, R. M. A.; McDonnell, L. A.; Amstalden, E.; Luxembourg, S. L.; Altelaar, A. F. M.; Piersma, S. R. *Appl. Surf. Sci.* **2006**, *252*, 6827−6835.

(2) Green, F. M.; Gilmore, I. S.; Seah, M. P. *J. Am. Soc. Mass Spectrom.* **2006**, *17*, 514−523.

(3) Carado, A.; Passarelli, M. K.; Kozole, J.; Wingate, J. E.; Winograd, N.; Loboda, A. V. *Anal. Chem.* **2008**, *80*, 7921−7929.

(4) Hill, R.; Blenkinsopp, P.; Thompson, S.; Vickerman, J.; Fletcher, J. S. *Surf. Interface Anal.* **2011**, *43*, 506−509.

(5) *MALDI MS, A Practical Guide to Instrumentation, Methods and Applications*; Hillenkamp, F., Peter-Katalinic, J., Eds.; Wiley-VCH: Weinheim, 2014.

(6) Satoh, T.; Sato, T.; Kubo, A.; Tamura, J. *J. Am. Soc. Mass Spectrom.* **2011**, *22*, 797−803.

(7) Larson, P. E.; Hammond, J. S.; Heeren, R. M. A.; Fisher, G. L. Method and Apparatus to Provide Parallel Acquisition of MS/MS Data. U.S. Patent 20150090874, 2015.

(8) Ogrinc Potočnik, N.; Porta, T.; Becker, M.; Heeren, R. M. A.; Ellis, S. R. *Rapid Commun. Mass Spectrom.* **2015**, *29*, 2195−2203.

(9) Van der Sar, A. M.; Abdallah, A. M.; Sparrius, M.; Reinders, E.; Vandenbroucke-Grauls, C. M. J. E.; Bitter, W. *Infection & Immunity* **2004**, *72*, 6306−6312.

(10) Nelson, K. A.; Daniels, G. J.; Fournie, J. W.; Hemmer, M. J. *J. Biomol. Techniques* **2013**, *24*, 119−127.

(11) Schueler, B.; Sander, P.; Reed, D. A. *Vacuum* **1990**, *41*, 1661−1664.

(12) Schueler, B. W. *Microsc., Microanal., Microstruct.* **1992**, *3*, 119−139.

(13) Sleno, L.; Volmer, D. A. *J. Mass Spectrom.* **2004**, *39*, 1091−1112.

(14) Amaya, K. R.; Monroe, E. B.; Sweedler, J. V.; Clayton, D. F. *Int. J. Mass Spectrom.* **2007**, *260*, 121−127.

(15) Shariatgorji, M.; Nilsson, A.; Goodwin, R. J. A.; Kallback, P.; Schintu, N.; Zhang, X.; Crossman, A. R.; Bezard, E.; Svenningsson, P.; Andren, P. E. *Neuron* **2014**, *84*, 697−707.

(16) He, X.; Huang, Y.; Li, B.; Gong, C.-X.; Schuchman, E. H. *Neurobiol. Aging* **2010**, *31*, 398−408.

(17) Chan, R. B.; Oliveira, T. G.; Cortes, E. P.; Honig, L. S.; Duff, K. E.; Small, S. A.; Wenk, M. R.; Shui, G.; Di Paolo, G. *J. Biol. Chem.* **2012**, *287*, 2678−2688.

(18) Jones, E. E.; Dworski, S.; Canals, D.; Casas, J.; Fabrias, G.; Schoenling, D.; Levade, T.; Denlinger, C.; Hannun, Y. A.; Medin, J. A.; Drake, R. R. *Anal. Chem.* **2014**, *86*, 8303−8311.

(19) George, J. M.; Jin, H.; Woods, W. S.; Clayton, D. F. *Neuron* **1995**, *15*, 361−372.

(20) Denisenko-Nehrbass, N. I.; Jarvis, E. D.; Scharff, C.; Nottebohm, F.; Mello, C. V. *Neuron* **2000**, *27*, 359−370.

(21) Innis, S. M. *J. Nutr.* **2007**, *137*, 855−859.

(22) Amaya, K. R.; Sweedler, J. V.; Clayton, D. F. *J. Neurochem.* **2011**, *118*, 499−511.

(23) Fisher, G. L.; Hammond, J. S.; Larson, P. E.; Bryan, S. R.; Heeren, R. M. A. *J. Vac. Sci. Technol. B* **2016**, *34*, Articleno. 03H126 DOI: 10.1116/1.4943568.

(24) Unpublished results of tandem MS imaging of surface precipitates on heat-treated poly(ethylene terephthalate) (PET). Line scan measurements of both MS^1 and MS^2 images, acquired simultaneously, reveal a lateral resolution ($\Delta l_{80/20}$) of < 200 nm.

(25) Harvey, D. J. *J. Am. Soc. Mass Spectrom.* **2005**, *16*, 280−290.

(26) McDonnell, L. A.; Heeren, R. M. A. *Mass Spectrom. Rev.* **2007**, *26*, 606−643.

(27) MacAleese, L.; Duursma, M. C.; Klerk, L. A.; Fisher, G. L.; Heeren, R. M. A. *J. Proteomics* **2011**, *74*, 993−1001.

(28) Cerruti, C. D.; Benabdellah, F.; Laprevote, O.; Touboul, D.; Brunelle, A. *Anal. Chem.* **2012**, *84*, 2164−2171.

(29) Vickerman, J.; Winograd, N. In *Cluster Secondary Ion Mass Spectrometry: Principles and Applications*; Mahoney, C., Ed.; John Wiley & Sons: Hoboken, NJ, 2013; pp 269−312.